Nanoscale

PAPER

View Article Online
View Journal | View Issue

Cite this: *Nanoscale*, 2017, **9**, 6808

The hot carrier diffusion coefficient of sub-10 nm virgin MoS_2: uncovered by non-contact optical probing

Pengyu Yuan, † Jing Liu, † Ridong Wang and Xinwei Wang *

We report a novel approach for non-contact simultaneous determination of the hot carrier diffusion coefficient (D) and interface thermal resistance (R) of sub-10 nm virgin mechanically exfoliated MoS_2 nanosheets on c-Si. The effect of hot carrier diffusion in heat conduction by photon excitation, diffusion, and recombination is identified by varying the heating spot size from 0.294 μm to 1.14 μm (radius) and probing the local temperature rise using Raman spectroscopy. R is determined as 4.46–7.66 × 10^{-8} K m^2 W^{-1}, indicating excellent contact between MoS_2 and c-Si. D is determined to be $1.18^{+0.30}_{-0.23}$, $1.07^{+0.37}_{-0.26}$, $1.20^{+0.34}_{-0.27}$ and $1.62^{+0.30}_{-0.23}$ cm^2 s^{-1} for 3.6 nm, 5.4 nm, 8.4 nm, and 9.0 nm thick MoS_2 samples, showing little dependence on the thickness. The hot carrier diffusion length (L_D) can be determined without knowledge of the hot carrier's life-time. The four samples L_D is determined as $0.344^{+0.041}_{-0.036}$ (3.6 nm), $0.327^{+0.052}_{-0.043}$ (5.4 nm), $0.346^{+0.046}_{-0.042}$ (8.4 nm), and $0.402^{+0.036}_{-0.030}$ μm (9.0 nm). Unlike previous methods that are implemented by making electrical contact and applying an electric field for D measurement, our technique has the advantage of being truly non-contact and non-invasive, and is able to characterize the electron diffusion behavior of virgin 2D materials. Also it points out that hot carrier diffusion needs to be taken into serious consideration in Raman-based thermal property characterization of 2D materials, especially under very tightly focused laser heating whose spot size is comparable to the hot carrier diffusion length.

Received 24th March 2017,
Accepted 19th April 2017

DOI: 10.1039/c7nr02089a

rsc.li/nanoscale

1. Introduction

Two-dimensional (2D) atomic materials such as graphene and transition metal dichalcogenides (TMDs) (*e.g.* MoS_2, WS_2, and $MoSe_2$) have attracted considerable attention because of their suitability for future electronic, piezoelectric and optoelectronic device applications.[1–4] Especially, TMDs are interesting for next generation devices because, in contrast to graphene, they are semiconductors with a tunable bandgap. For instance, a single layer of MoS_2 has a direct band gap of 1.8 eV compared with the indirect band gap of 1.29 eV in bulk.[5,6] This thickness-dependent band gap makes MoS_2 suitable for potential photo-detection and optoelectronic applications and could be of interest for achieving a higher power conversion efficiency in traditional silicon solar cells.[7,8]

As investigated, electrons or holes in semiconductor materials with higher energies compared with the Fermi energy are called hot carriers. They can be generated electrically by high electrical fields or by injection through a barrier. Carrier mobility (μ) describes the motion of electrons under electric fields. Hot carriers can also be produced optically by photons with excessive energy. In this electric field free environment, the carrier diffusion coefficient (D) is more common for the description of charge movement. The diffusion is caused and directed by the concentration gradient instead of the electric field. The hot carrier's behavior plays a significant role in modern semiconductor science. Hot carrier phenomena (*e.g.* hot carrier effects) are important in the operation of many semiconductor devices such as laser diodes, solar cells, short-channel field-effect transistors (FETs), and high-speed devices like ultrafast photodetectors and hot-electron transistors.[8–11] Like free electrons in metals, the transport of hot carriers is affected by various interactions between carriers and other elementary excitations (*e.g.* electron–phonon coupling, electron–electron collisions, the capture of carriers by impurities, exciton interactions, *etc.*) in semiconductor materials.[12] So the study of hot carrier transport properties provides important information about the scattering processes in semiconductors. Additionally, extensive work has been done on hot carrier in graphene with measured D as high as 11 000 cm^2 s^{-1},[8,13–15] while reports on MoS_2 are scarce.[16]

Department of Mechanical Engineering, Iowa State University, 271 Applied Science Complex II, Ames, IA 50011, USA. E-mail: xwang3@iastate.edu; Tel: +1-515-294-8023

† These authors contributed equally to this work.

To date, several methods have been developed and applied to study hot carrier transport properties (mobility or diffusion coefficient) under either high electric fields or photon-injection. The majority of works focus on electrically generated hot carriers. However, the experimentally measured carrier mobility by different methods varies by almost an order of magnitude. This large discrepancy could result from many factors: the charge impurity scattering, electron–phonon interaction, and screening by the surrounding dielectric environment.[17] Besides, even the suppression of Coulomb scattering and modification of phonon dispersion from the device preparation process can introduce strong effects. For example, the mobility of mechanically exfoliated multilayered (15–90 nm) MoS_2 FETs with SiO_2 as a high-κ dielectric is reported in the range of 30–60 $cm^2\ V^{-1}\ s^{-1}$ in a four-probe configuration.[18] The exfoliated multilayered (8–40 nm) MoS_2 FETs on SiO_2 have a carrier mobility from 10 to 50 $cm^2\ V^{-1}\ s^{-1}$ by two-probe measurements for back-gated structures.[19] In contrast, the top-gated MoS_2 FETs with HfO_2 demonstrated a mobility up to about 200 $cm^2\ V^{-1}\ s^{-1}$, which is even higher than that of bandgap-engineered graphene.[16] During those measurements, they have to apply a voltage to the electric contact to control the electron population in the material. However, the question is still open regarding the role of the electrical contacts causing screening disorder in multilayered MoS_2 FETs.[18,20] The use of a high-κ gate dielectric in a top-gated device is shown to boost the carrier mobility which is caused by screening of impurities by the dielectric and/or modifications of the MoS_2 phonons in the top-gated sample.[16] Besides, the nanosheets could be potentially modified and even destroyed during the device preparation process (*e.g.* pattern electrical contacts using electron-beam lithography), especially for ultra-thin samples.[21–23] So optical-based measurements of hot carriers transport properties could give us more in-depth understanding of virgin 2D materials. For MoS_2, very little optical-based studies have been reported on electron transport. Kumar *et al.* used transient absorption microscopy to determine the diffusion coefficient of the thermalized electron (hot electron) of bulk MoS_2 crystal to be around 4.2 $cm^2\ s^{-1}$.[24] For multilayered MoS_2, Wang *et al.* employed a spatially and temporally resolved pump–probe technique and obtained the carrier diffusion coefficient as 20 ± 10 $cm^2\ s^{-1}$ for few-layered (1.5–2.2 nm) MoS_2 on Si.[25]

In this work, we develop a non-contact technique to directly measure the hot carrier diffusion coefficient. By varying the laser heating spot size, the effect of hot carrier diffusion is identified by the local temperature rise, which is probed by using Raman spectroscopy. Unlike previous studies by electrical techniques where the mobility of carriers was measured under an external electric field, we characterize the hot carrier diffusion caused by the density gradient without making any electrical contact with the sample or exposing it to an electric field. Therefore this technique eliminates the detrimental effect of direct contact and measures the intrinsic carrier transport properties of materials. We deduce the hot carrier diffusion coefficient as 1.07–1.62 $cm^2\ s^{-1}$ and the interface thermal resistance as 4.42×10^{-8}–7.66×10^{-8} $K\ m^2\ W^{-1}$ for mechanically exfoliated sub-10 nm virgin MoS_2 on c-Si substrate. This technique could be a very promising tool for investigating the hot carrier transport of various virgin 2D materials.

2. Physical principles

The schematic in Fig. 1(a) shows the physical principles of our non-contact technique. Here we use a CW (continuous-wave) 532 nm (E = 2.33 eV) laser to excite the MoS_2/c-Si structure. Because the excitation energy E is greater than the band gap of MoS_2 (E_g = 1.29–1.80 eV) and c-Si (E_g = 1.15 eV), the electrons (e) are excited by the absorbed photons to the conduction band, leaving holes (h) in the valence band. Part of the photon energy $\Delta E = (E - E_g)$ of hot carriers is quickly dissipated to other electrons and the lattice by a fast non-radiative process. This occurs very quickly (about 10^{-12} s) so that we can neglect carrier diffusion effects during this process. The remaining photon energy (E_g) is carried by electrons. They store this photon energy and diffuse out of the excitation spot before recombining with holes, leading to a significantly wider thermal source spatial redistribution as a result of diffusion. Due to the Coulomb attraction, the excited electrons and holes move together as e–h pairs in this diffusion process. This diffusion process time is typically nanoseconds and diffusion cannot be neglected.[26] Since both the multilayered MoS_2 and c-Si have an indirect bandgap, the radiative recombination of carriers is greatly restricted by crystal momentum conservation. So the excited hot electrons would release the laser energy *via* non-radiative recombination with holes by exciting phonons. The energy of these phonons in MoS_2 dissipates within the 2D nanosheet and through layers down to substrate to raise the temperature, eventually reaching thermal equilibrium with the electrons. The generation and diffusion of heat and hot carriers in the sample are governed by two partial differential equations in steady state ($\partial N/\partial t = 0$).[27,28] The first one is the carrier diffusion equation to determine the hot carrier concentration $\Delta N(\boldsymbol{r},t)$ (cm^{-3}):

$$D\nabla^2\Delta N - \frac{\Delta N}{\tau} + \frac{\partial n_0}{\partial T}\frac{\Delta T}{\tau} + \Phi\alpha = 0, \quad (1)$$

where D ($cm^2\ s^{-1}$), τ (s) and Φ (photons per cm^3 per s) are the carrier diffusion coefficient, the electron–hole recombination time of MoS_2 and the incident photon flux of the laser source. α is the optical absorption coefficient of the MoS_2 nanosheets. n_0 (cm^{-3}) is the equilibrium free-carrier density at temperature T. The first term on the left side is about the carrier diffusion and the second term: $\Delta N/\tau$ represents the electron–hole recombination. The thermal activation term $(\partial n_0/\partial T)\Delta T/\tau$ is related to the carrier creation due to the temperature rise. It is negligible under a relatively low-temperature rise and in small free-carrier density cases.[27,29] In our experiment, for the 3.6 nm thick sample, the temperature rise under a 20× objective is only 1.0 $K\ mW^{-1}$ (temperature rises for the other samples

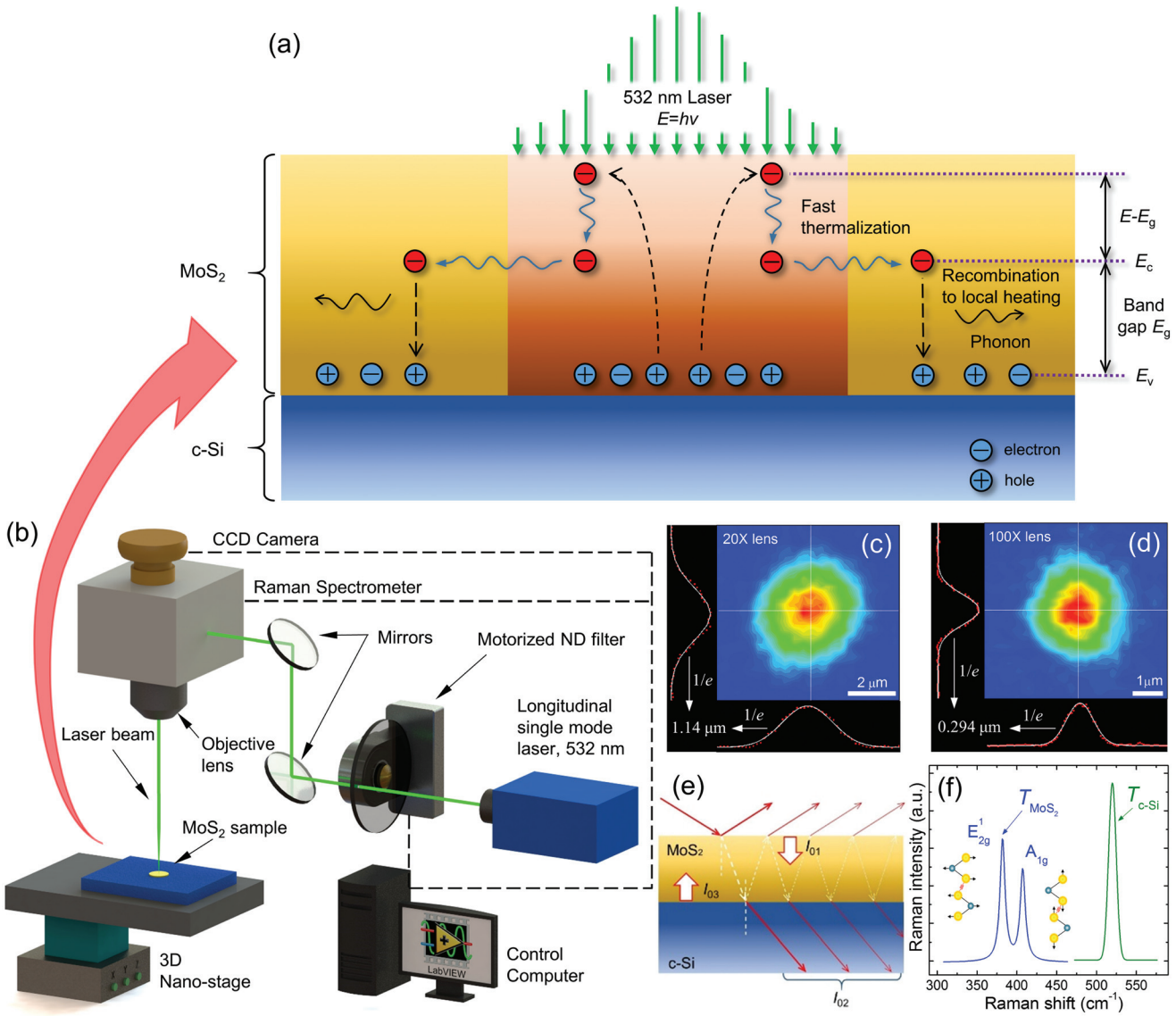

Fig. 1 (a) Schematic of MoS_2 under a CW 532 nm (2.33 eV) laser illumination (not to scale). The photons generate hot carriers in the MoS_2 sample by exciting electrons (e) to the conduction band, leaving holes (h) in the valance band. The hot carriers transfer part of the photon energy ($E - E_g$) to the lattice thermal energy by fast thermalization, diffuse out of the direct laser heating region to the low population region, and then recombine with holes to lose the rest part of the photon energy (E_g) through phonon emission (carrier-phonon scattering). We use two objective lenses to achieve different laser spot size heating with simultaneous Raman probing to detect the local temperature rise. (b) Schematic of the experimental setup for micro-Raman experiment of MoS_2/c-Si sample. The sample is illuminated by the laser and the Raman signals of MoS_2 and c-Si are excited by the same laser and collected by a confocal Raman spectrometer (Voyage, B&W Tek, Inc.) with a spectral resolution of 1.05–1.99 cm^{-1}. The laser power is adjusted by a motorized ND filter. The spectrometer and ND filter are controlled by LabVIEW-based software. The MoS_2 nanosheets absorb laser energy and dissipate heat to the c-Si substrate through their interface. (c), (d) The spatial energy distribution of the laser beam and spot size are measured with a CCD camera (Olympus DP-26, Olympus Optical Co., Ltd). The red points in (c) and (d) are laser beam spot size data taken from the CCD camera images. The white curves are fits to the Gaussians. The laser beam radius (at e^{-1}) on the sample is determined as 1.14 μm under 20× objective, and 0.294 μm under 100×. (e) When laser beam irradiates the sample surface, multiple reflections happen at the interface between MoS_2 and c-Si. The transmitted power at the top surface (I_{01}), the transmitted power in c-Si top surface (I_{02}) and the reflected power at the bottom surface (I_{03}) of MoS_2 are calculated out according to the Transfer Matrix Method (TMM).[32] (f) Temperatures of both MoS_2 and c-Si can be determined simultaneously by their Raman spectra. Here we choose the E^1_{2g} mode to evaluate the MoS_2 temperature.

under different lenses are summarized in Table 1). Besides, the free carrier density at equilibrium could be given as $n_0 = N_s \exp(-E_g/2k_BT)$, where N_s is the number density of effectively available states. It is in the order of 10^{19} cm^{-3} at room temperature and increases with temperature. k_B is the Boltzmann's constant. E_g is the band gap energy. At room temperature, $k_BT = 0.026$ eV. Since $E_g = 1.3$ eV, we have $k_BT \ll E_g$. This leads to a very small n_0 (room temperature) to neglect the thermal

Table 1 Summary of Raman experiment results of four MoS_2 samples. The power coefficients (χ_P) under different objective lenses from both E^1_{2g} and A_{1g} modes of MoS_2 and the substrate c-Si, and temperature coefficients (χ_T) from both E^1_{2g} and A_{1g} modes. The Raman/laser intensity weighted average temperature rise per unit laser power ($\Delta\bar{T}_{MoS_2}$) and temperature difference [$\Delta\bar{T} = (\Delta\bar{T}_{MoS_2} - \Delta\bar{T}_{c\text{-}Si})$] between MoS_2 and c-Si under different objective lenses by using the Raman results of E^1_{2g} mode of MoS_2

Sample thickness:			3.6 nm	5.4 nm	8.4 nm	9.0 nm
$\chi_{P(20\times)}$ (cm^{-1} mW^{-1})	MoS_2	E^1_{2g}	$-(0.029 \pm 6.4 \times 10^{-4})$	$-(0.024 \pm 1.1 \times 10^{-3})$	$-(0.030 \pm 8.5 \times 10^{-4})$	$-(0.030 \pm 9.4 \times 10^{-4})$
		A_{1g}	$-(0.027 \pm 7.0 \times 10^{-4})$	$-(0.025 \pm 8.5 \times 10^{-3})$	$-(0.025 \pm 1.5 \times 10^{-3})$	$-(0.032 \pm 9.6 \times 10^{-4})$
	c-Si		$-(0.008 \pm 3.0 \times 10^{-4})$	$-(0.007 \pm 2.2 \times 10^{-4})$	$-(0.011 \pm 4.2 \times 10^{-4})$	$-(0.010 \pm 2.7 \times 10^{-4})$
$\chi_{P(100\times)}$ (cm^{-1} mW^{-1})	MoS_2	E^1_{2g}	$-(0.151 \pm 3.8 \times 10^{-3})$	$-(0.142 \pm 6.2 \times 10^{-3})$	$-(0.163 \pm 7.4 \times 10^{-3})$	$-(0.154 \pm 4.2 \times 10^{-3})$
		A_{1g}	$-(0.151 \pm 4.1 \times 10^{-3})$	$-(0.163 \pm 8.5 \times 10^{-3})$	$-(0.163 \pm 8.9 \times 10^{-3})$	$-(0.152 \pm 4.9 \times 10^{-3})$
	c-Si		$-(0.012 \pm 3.0 \times 10^{-4})$	$-(0.016 \pm 5.2 \times 10^{-4})$	$-(0.026 \pm 9.0 \times 10^{-4})$	$-(0.013 \pm 5.3 \times 10^{-4})$
$\chi_{T(50\times)}$ (cm^{-1} K^{-1})	E^1_{2g}		$-(0.029 \pm 1.3 \times 10^{-3})$	$-(0.020 \pm 1.2 \times 10^{-3})$	$-(0.016 \pm 7.0 \times 10^{-4})$	$-(0.024 \pm 7.6 \times 10^{-4})$
	A_{1g}		$-(0.028 \pm 1.1 \times 10^{-3})$	$-(0.018 \pm 1.3 \times 10^{-3})$	$-(0.014 \pm 9.0 \times 10^{-4})$	$-(0.021 \pm 1.1 \times 10^{-3})$
$\Delta\bar{T}_{MoS_2}$ (K mW^{-1})	20×		$-(1.00 \pm 0.05)$	$-(1.16 \pm 0.08)$	$-(1.85 \pm 0.10)$	$-(1.26 \pm 0.06)$
	100×		$-(5.21 \pm 0.26)$	$-(6.86 \pm 0.49)$	$-(9.96 \pm 0.62)$	$-(6.42 \pm 0.27)$
$\Delta\bar{T} = \Delta\bar{T}_{MoS_2} - \Delta\bar{T}_{c\text{-}Si}$ (K mW^{-1})	20×		$-(0.71 \pm 0.05)$	$-(0.89 \pm 0.06)$	$-(1.41 \pm 0.07)$	$-(0.89 \pm 0.04)$
	100×		$-(4.74 \pm 0.24)$	$-(6.27 \pm 0.45)$	$-(8.94 \pm 0.55)$	$-(5.92 \pm 0.25)$

activation term. The last term $\Phi\alpha$ is the carrier photogeneration source term. In our work, the MoS_2 film is very thin (sub-10 nm) compared with its lateral dimension (4–12 μm), so the hot carrier gradient in the thickness direction is neglected. Therefore, eqn (1) only considers the in-plane direction diffusion.

The second equation is the thermal diffusion equation which involves the free carrier density since the non-radiative recombination is a heat source:

$$k\nabla^2\Delta T + (h\nu - E_g)\Phi\alpha + \frac{E_g\Delta N}{\tau} = 0, \quad (2)$$

where $\Delta T(\boldsymbol{r},t)$ (K), k (W m^{-1} K^{-1}) and E_g (eV) are the temperature rise, the thermal conductivity and the bandgap energy of the multilayered MoS_2. And $h\nu$ (eV) is the photon energy of the laser source. The second term of eqn (2), $(h\nu - E_g)\Phi\alpha$, which is proportional to $h\nu - E_g$, represents the heat generation due to photo-generated carriers giving off the excess energy to the MoS_2 lattice. The term $E_g\Delta N/\tau$ contains the carrier concentration representing the heat generation through the non-radiative recombination of free carriers.

The hot electrons diffuse in the sample until they recombine with holes through non-radiative transition. Therefore, the real heating area is not simply the laser irradiating area. Instead, it is strongly affected by the hot carrier diffusion length ($L_D = \sqrt{\tau D}$) of the electrons. When the laser heating spot size (radius: 0.294 μm to 1.14 μm) is comparable to the carrier diffusion length and the laser heating spot size is relatively small, this effect becomes more prominent. If the laser heating spot size is sufficiently large, the hot carrier diffusion will have less or negligible effect on the heating area. For multilayered MoS_2, the hot carrier diffusion length is in the order of 0.1 μm.[16,30] So we could observe different heating phenomena in MoS_2 by changing the laser heating spot size. However, the c-Si used in this experiment is single-side polished silicon wafer (p-doped, (100)-oriented, 0–100 Ω cm resistivity, ~0.335 μm thickness) from University Wafer Company (Boston, MA). The diffusion length of this p-type Si is around 700 μm (ref. 31), which is much larger than our laser heating spot size. Generally, bulk and surface recombination mechanisms coexist. Nevertheless, we only consider the bulk recombination process here. The physics can be explained as below. First, consider the c-Si surface area of the MoS_2/c-Si interface. MoS_2 could be thought of as native n-doping due to its sulfur vacancies.[32] So the MoS_2/c-Si structure is just one p–n junction, and the depletion region of that has been found to considerably reduce the surface recombination rate.[33] Then, for the remaining c-Si surface, its native oxide layer could be the predominant passivating layer which can also significantly reduce the surface recombination rate.[33] So we could neglect the effect of the carriers surface recombination for the diffusion process. In this case, the transmitted laser energy only heats the c-Si substrate by the fast thermalization process ($\Delta E = E - E_g|_{c\text{-}Si}$) because the hot carriers with the remaining photon energy ($E_g|_{c\text{-}Si}$) diffuse such a long distance that a uniform heating of the overall Si substrate is induced. As a result, the measured temperature rise of MoS_2 (by Raman spectrum) is determined by the hot carrier diffusion and the MoS_2/c-Si interface thermal resistance. Eqn (1) and (2) are solved to analyze the experimental results and determine the hot electron diffusion coefficient and the interface thermal resistance/conductance. In our work, the temperature difference between MoS_2 and Si is determined and used. This treatment has taken into full consideration the temperature rise effect of the c-Si substrate.

3. Experimental details

Raman experiments are conducted by using a confocal Raman system that consists of a Raman spectrometer (Voyage™, B&W Tek, Inc.) and a microscope (Olympus BX53). We use a longi-

tudinal single mode laser of 532 nm as shown in Fig. 1(b). The laser is introduced to the Raman system and its power is adjusted by a motorized neutral-density (ND) filter system (CONEX-NSR1 and NSND-5, Newport Corporation). We use a 3D piezo-actuated nano-stage (MAX313D, Thorlabs, Inc.) with a resolution of 5 nm to search for and identify the MoS_2 sample on the c-Si under a microscope. The laser beam is focused on a specific area of the samples (detailed in Fig. 2) and the laser power is varied to introduce different heating levels in the MoS_2 samples. The optically generated heat is dissipated away across the MoS_2/c-Si interface to the substrate. During the experiments, both the Raman spectrometer and the motorized ND filter are controlled by LabVIEW-based software on a computer. The Raman spectrometer could collect and store the spectra for each energy level automatically after the ND filter is set. This significantly shortens the experiment time, reduces the external disturbance, and improves the precision and accuracy of the experiment. We use the Raman spectrometer to measure the temperature rise of MoS_2 and c-Si. Based on the temperature rise and the absorbed laser power, we can directly determine the hot carrier diffusion coefficient and interfacial thermal resistance.

Shown in Fig. 1(c) and (d) are the laser energy distribution contours under 20× and 100× objective lenses for focused laser spot images obtained by using a CCD camera. The beam size at the focal plane is measured by using the CCD camera, where there is enough irradiance to have a suitable signal-to-noise ratio without saturating the camera, and the beam lineout is fitted with a Gaussian function [the white curves in Fig. 1(c) and (d)] for both x and y directions to take the average as final results. For the CCD camera, the pixel size under 20×, 50×, and 100× lenses is 0.347, 0.123 and 0.069 μm per pixel, respectively. Then the Gaussian beam spot size r_0 (at e^{-1} peak value) under 20×, 50×, and 100× lenses is 1.14 ± 0.01, 0.531 ± 0.006, and 0.294 ± 0.003 μm, respectively. When the laser beam irradiates the sample surface, multiple reflections happen within the MoS_2 film. According to the Transfer Matrix Method (TMM)[34] and the complex refractive index of two materials,[35] we could determine the transmitted power at the top surface (I_{01}), the transmitted power in c-Si top surface (I_{02}) and the reflected power at the bottom surface (I_{03}) of MoS_2. Note that we assume that the complex refractive index of MoS_2 is constant because it has been found that the complex refractive index has little change with the sample's thickness for our sample thickness range.[6]

4. Results and discussion

4.1 Structure of MoS_2 film on c-Si

We prepare the sub-10 nm thick multilayered MoS_2 samples by micromechanical cleavage from their parent bulk MoS_2 crystals (429MS-AB, molybdenum disulfide, small crystals from the USA, SPI Suppliers). Among atomically thin nanosheets preparation methods such as chemical vapor deposition and liquid exfoliation, mechanical exfoliation is widely used and is the most efficient way to produce clean, high quality atomically thin structures layered materials for fundamental studies.[36] As in the typical micromechanical exfoliation process, ordinary adhesive Scotch tape and gel film (Gel-Film, PF-20/1.5-X4,

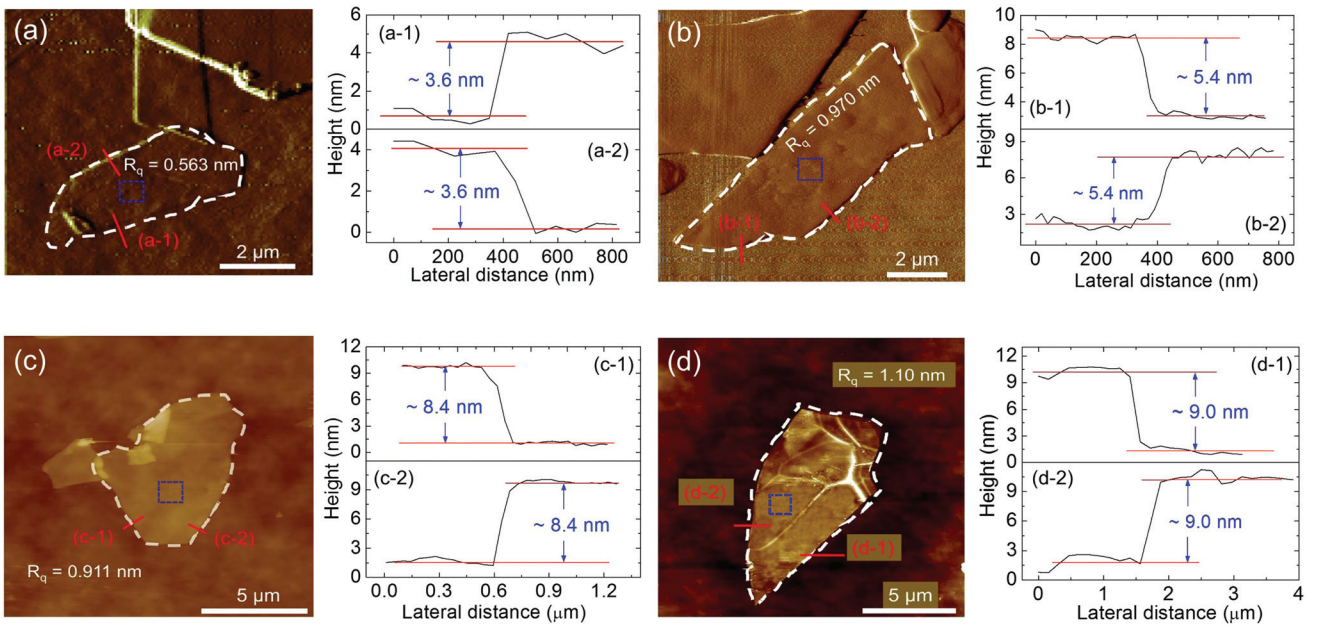

Fig. 2 AFM measurement results of four MoS_2 samples. (a)–(d) AFM images of four MoS_2 nanosheets. The white dashed circled area indicates the MoS_2 sample. The blue dashed box indicates the sample roughness study area. The bottom two figures [*e.g.* (a-1) and (a-2)] in each panel show the step height measurement results from the substrate to the sample. The measurement is along the red lines in the upper figure. The R_q value in each AFM image indicates the RMS roughness.

Gel-Pak) are used to prepare layered MoS_2 nanosheets on a freshly cleaned c-Si substrate.[35,37] The lateral size of layered MoS_2 nanosheets ranges from 4 to 12 μm. We use an optical microscope, an atomic force microscope (AFM) (Model MMAFM-2, Digital Instruments, CA, USA) and Raman spectroscopy to identify and locate the MoS_2 nanosheets.

Fig. 2 shows AFM scan images of the four studied MoS_2 samples on the c-Si substrate. The samples have a thickness of 3.6 nm, 5.4 nm, 8.4 nm, and 9.0 nm, respectively. During AFM imaging, instead of using tapping or other modes, we choose contact mode in order to reduce the thickness measurement noise.[38] In Fig. 2, for each sample, the sample area is marked by the dashed white curves. Two red lines indicate the edges for height measurements, and the measurement results are shown in the two right-hand-side figures for each sample. The blue box in each sample AFM image shows the area where the laser is focused during Raman experiment. The sample surface roughness is evaluated as well. The 3.6 nm thick sample has a root-mean-square (RMS) roughness (R_q) of 0.563 nm. As the thickness increases, RMS roughness increases: the R_q value for the 5.4 nm, 8.4 nm, and 9.0 nm thick sample is 0.970 nm, 0.911 nm, and 1.10 nm, respectively. This is probably due to possible wrinkles or ripples in the samples. Also, the substrate (c-Si) has a R_q of 0.09 nm, confirming its atomically smooth surface.

4.2 Steady thermal response of MoS_2 and c-Si under laser heating of different spot sizes

In our experiments, for all the four samples, eight room-temperature Raman spectra are collected at laser power (P) spanning from 2.49 to 11.9 mW (the corresponding average power density $P/\pi r_0^2$ is 0.942 to 4.50 MW cm^{-2}) under a 100× objective and from 6.83 to 32.8 mW ($P/\pi r_0^2$ from 0.167 to 8.03 MW cm^{-2}) under a 20× objective. Note that this laser power is the level just before the laser enters the MoS_2 sample. This heating power variation is designed to study the Raman spectrum change under optical heating, and this could also significantly suppress the experiment noise of a single laser power experiment. To avoid damage to the sample and to stay within the linear temperature-dependence range for Raman properties, we try to keep the excitation laser power as low as possible. The Raman spectra of MoS_2 nanosheets taken with a 532 nm wavelength laser show two prominent phonon modes, E^1_{2g} and A_{1g}. The E^1_{2g} mode is associated with the in-plane opposite vibration of two sulfur atoms with respect to the molybdenum atom, whereas the A_{1g} mode is associated with the out-of-plane vibration of only sulfur atoms in opposite directions,[39] as depicted in the insets of Fig. 3(a). Five representative room temperature Raman spectra under 100× objective lens and their corresponding Lorentzian fits collected from the 3.6 nm thick MoS_2 sample are shown in Fig. 3(a), where both E^1_{2g} and A_{1g} modes shift left (red-shift) linearly with increased laser power and the peak position shifts are visible as $\Delta\omega$|(2.49 mW–11.9 mW). These changes indicate that the local temperature of the sample surface becomes higher under a higher laser power. We use two objective lenses to generate different optical heating phenomena. Fig. 3(c) and (d) show the Raman shift for the two vibration modes as a function of incident laser power under 20× and 100× objective lenses, respectively. In our specified laser power range, it is observed that the Raman shift linearly depends on the laser power by $\Delta\omega = \omega(P_2) - \omega(P_1) = \chi_P(P_2 - P_1) = \chi_P\Delta P$. χ_P is the first-order laser power coefficient for two vibration modes of MoS_2 and c-Si, and P is the laser power. For this 3.6 nm thick sample, the fitted χ_P for E^1_{2g} and A_{1g} modes are quite close, $-(0.151 \pm 3.8 \times 10^{-3})$ cm^{-1} mW^{-1} and $-(0.151 \pm 4.1 \times 10^{-3})$ cm^{-1} mW^{-1} under a 100× objective, and $-(0.029 \pm 6.0 \times 10^{-4})$ cm^{-1} mW^{-1} and $-(0.027 \pm 7.0 \times 10^{-4})$ cm^{-1} mW^{-1} under a 20× objective, respectively. Note that the laser power coefficients for the two vibration modes under the 100× objective are higher than those under the 20× objective. This is because the temperature rise determined by Raman spectra under the 100× objective increases more rapidly than that under the 20× objective due to the larger power density under the 100× objective lens. The fitted χ_P of c-Si for this 3.6 nm thick MoS_2 sample are $-(0.008 \pm 3.0 \times 10^{-3})$ cm^{-1} mW^{-1} (Fig. 3(e)) and $-(0.151 \pm 4 \times 10^{-3})$ cm^{-1} mW^{-1} (Fig. 3(f)) under 20× and 100× objectives, respectively.

We also conduct the temperature calibration experiment for MoS_2 and c-Si to determine the local temperature rise during the above experiment. The calibration experiment is carefully performed for each sample considering the possible sample-to-sample difference. To keep the entire MoS_2 nanosheets and the c-Si substrate at the same temperature, we place the MoS_2/c-Si sample on a heat stage and control the sample's temperature by a voltage transformer that powers the heater, and monitor the temperature by a thermocouple. The Raman spectra of both MoS_2 and c-Si are collected after the sample's temperature reaches a steady reading. Fig. 3(b) shows five representative Raman spectra and their corresponding Lorentzian fits with the temperature ranging from 297 to 398 K under a 50× objective lens. The power of the incident laser power is maintained low enough to not increase much the temperature rise at the irradiated spot (1.10 mW before entering the sample). The Raman shift of both E^1_{2g} and A_{1g} modes decreases with increased temperature, which is visible as $\Delta\omega$|(297 K–398 K). The temperature dependence of both E^1_{2g} and A_{1g} modes of MoS_2 and c-Si measured between 297 and 398 K is depicted in Fig. 3(b). The Raman shift for both E^1_{2g} and A_{1g} modes decreases with increased global temperature for all cases and exhibits linear temperature dependence in the range used in our experiment.

We could describe the Raman peak position as a function of temperature as $\Delta\omega = \omega(T_2) - \omega(T_1) = \chi_T(T_2 - T_1) = \chi_T\Delta T$. χ_T is the first-order temperature coefficient for MoS_2 vibration modes and c-Si, and T is temperature. Here, we do not consider the higher order temperature coefficients because these terms are only significant at a higher temperature about 570 K and above.[40,41] For the 3.6 nm thick MoS_2 sample, as shown in Fig. 3(g), the extracted χ_T values are $-(0.029 \pm 1 \times 10^{-3})$ cm^{-1} K^{-1} and $-(0.028 \pm 1 \times 10^{-3})$ cm^{-1} K^{-1} for E^1_{2g} and A_{1g} modes, and $-(0.026 \pm 1 \times 10^{-3})$ cm^{-1} K^{-1} for the c-Si substrate.

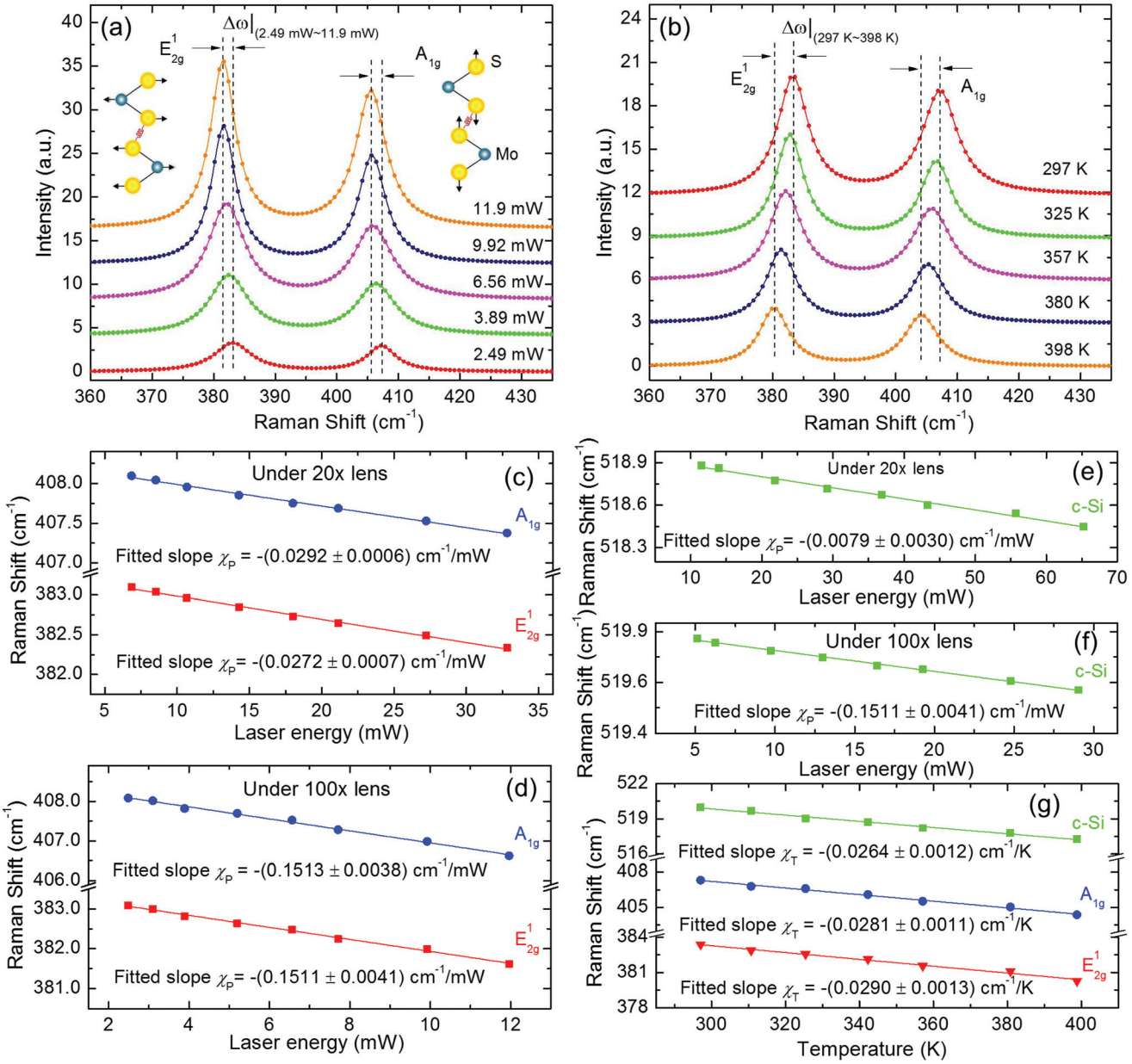

Fig. 3 The Lorentzian-fit Raman spectra of MoS_2 nanosheets. The sample with a thickness of 3.6 nm is used as an example to illustrate the micro-Raman results of hot carrier diffusion coefficient study and Raman temperature calibration experiment. (a) Five representative Raman spectra of MoS_2 at increased excitation laser power under 100× objective in ambient environment. Spectra are vertically shifted for clarity purpose. When the laser power increases, the local temperature increases. The Raman shifts for two modes are visible as $\Delta\omega$|(2.49 mW–11.9 mW). The Raman shift for A_{1g} and E^1_{2g} modes of MoS_2 as a function of laser power under 20× and 100× objectives are shown in (c) and (d), respectively. The Raman shift for c-Si as a function of laser power under 20× and 100× objective lenses are shown in (e) and (f), respectively. Fitting results (solid lines) for linear power coefficients χ_P are shown in these figures. (b) Five representative Raman spectra of MoS_2 collected at 297, 325, 357, 380 and 398 K under 50× objective during Raman temperature coefficient calibration experiment. Spectra are vertically shifted for clarity purpose. When the global temperature increases, the Raman shift for two modes are visible as $\Delta\omega$|(297 K–398 K). (g) The Raman shift for A_{1g} and E^1_{2g} modes of MoS_2 and c-Si as a function of temperature in calibration experiment. Fitting results (solid lines) for linear temperature coefficients χ_T are shown in the figure.

The temperature coefficients of all four samples are summarized in Table 1. The temperature-dependent changes in the Raman spectra are due to the anharmonic terms in the lattice potential energy, mediated by phonon–phonon interactions.[42] We note that for the 3.6 nm MoS_2 sample, the χ_T value from E^1_{2g} mode (-0.029 cm^{-1} K^{-1}) is slightly (3%) larger than that from A_{1g} mode (-0.028 cm^{-1} K^{-1}). The difference in χ_T value between those two modes becomes larger for the other three samples (*e.g.* χ_T of E^1_{2g} mode is ~14% larger than that of A_{1g} mode for the 9.0 nm sample). It makes sense that the out-of-plane A_{1g} mode shows a weaker temperature response for all these four multilayer MoS_2 samples, where there are interlayer

interactions restricting the vibrations away from the basal plane. And this restriction increases with increased layer number. The in-plane E^1_{2g} mode will be less affected by the interlayer interactions and weakly affected by the substrate,[41] so we use the Raman results from this vibration mode as the properties to evaluate the interface thermal resistance and the hot carrier diffusion coefficient.

In our experiment, the MoS_2/c-Si samples are firmly placed on a 3D nano-stage and the same point of each sample (as marked in Fig. 2 with dashed blue box) is measured during the entire experiments. This treatment could eliminate any possible location-to-location structure variation and temperature coefficient variation. For each MoS_2 sample, the average temperature rise per unit laser power ($\Delta\bar{T}_{20\times}$ and $\Delta\bar{T}_{100\times}$) could be experimentally obtained by $\Delta\bar{T}_{MoS_2 \text{ or c-Si}} = \chi_P\chi_T^{-1}$ (K mW^{-1}). And this value for the four MoS_2 samples is summarized in Table 1. The use of $\Delta\bar{T}$ instead of direct temperature rise ΔT (K) for the determination of D and R is to avoid artificial shifts of peak position resulting from calibration errors of two different objectives. Generally, a higher $\Delta\bar{T}_{MoS_2}$ is induced for a thicker sample because a thicker sample comes with a higher absorbance level. This results in a higher temperature rise in MoS_2 to transfer the heat across the interface down to the substrate. However, from Table 1, the temperature rise of the 9 nm MoS_2 (6.42 K at 100×) is lower than that of 8.4 nm MoS_2 (9.96 K at 100×). This is caused by lower interface thermal resistance (R) of 9.0 nm MoS_2 sample: the R for the 9.0 nm and 8.4 nm MoS_2 sample is 4.46×10^{-8} and 7.66×10^{-8} K m^2 W^{-1}, respectively (from Table 2). So there is more heat going into the substrate from the MoS_2 film for 9.0 nm sample. For the 3.6 nm thick MoS_2 sample, the highest temperature rise of the MoS_2 film and c-Si we have heated to is around 33 K and 10 K under the 20× objective, respectively, and around 62 K and 5.6 K under the 100× objective, respectively.

The heat transfer across the MoS_2/c-Si structure could be described by $\Delta q = A(T_{MoS_2} - T_{Si})/R$ (A is the heating area, Δq is the net heat flow). So the temperature difference between MoS_2 film and c-Si should be proportional to the inverse of the heating spot area. However, our results show that it is significantly different from this prediction, indicating the hot carrier diffusion effect. Taking the 3.6 nm MoS_2 as an example, under the 20× objective, the measured temperature difference per mW laser heating is 0.71 K. Under the 100× objective, the laser heating spot size is 6.6% of that under the 20× objective. As a result, we expect that the temperature rise difference is around 10.7 K under the 100× objective. But our measurement only gives a temperature rise difference of 4.74 K mW^{-1} under the 100× objective. This strongly indicates that the hot carriers diffuse out of the heating region, make the effective heating spot size bigger than the laser spot, and reduce the temperature difference.

Table 2 The summary of the calculated hot electron diffusion coefficient (D) and the interface thermal resistance (R) from the 3D numerical modeling and data fitting, and the corresponding electron mobility (μ) and electron diffusion length (L_D)

Sample thickness	R (10^{-8} K m^2 W^{-1})	D (cm^2 s^{-1})	μ (cm^2 V^{-1} s^{-1})	L_D (μm)
3.6 nm	$6.15^{+0.25}_{-0.25}$	$1.18^{+0.30}_{-0.23}$	$47.4^{+11.9}_{-9.38}$	$0.344^{+0.041}_{-0.036}$
5.4 nm	$6.27^{+0.38}_{-0.38}$	$1.07^{+0.37}_{-0.26}$	$42.7^{+14.7}_{-10.5}$	$0.327^{+0.052}_{-0.043}$
8.4 nm	$7.66^{+0.37}_{-0.36}$	$1.20^{+0.34}_{-0.27}$	$47.9^{+13.5}_{-10.8}$	$0.346^{+0.046}_{-0.042}$
9.0 nm	$4.42^{+0.17}_{-0.17}$	$1.62^{+0.30}_{-0.23}$	$64.8^{+12.2}_{-9.36}$	$0.402^{+0.036}_{-0.030}$

4.3 Determination of the hot carrier diffusion coefficient

Then we conduct a 3D numerical modeling based on the finite volume method to calculate the temperature rise to determine the hot carrier diffusion coefficient (D) and the interface thermal resistance (R). The model calculation size of the substrate has a radius and thickness of 50 μm. The MoS_2 sample has the actual size and thickness as those in the experiment. The smallest mesh size along the thickness direction is 0.1 nm and increases from the MoS_2 surface to the substrate with an increasing ratio of 1.02. The smallest mesh size is 1 nm in the radial direction and also increases with a ratio of 1.02. In our modeling, in the in-plane and cross-plane directions, we take $k_\parallel$ = 52 W m^{-1} K^{-1} (ref. 40) and $k_\perp$ = 2 W m^{-1} K^{-1},[43] $k_{c\text{-}Si}$ = 148 W m^{-1} K^{-1}.[44] P = 1 mW is the excitation laser energy before entering the sample. The thickness dependent bandgap of MoS_2 thin film has been investigated,[6] and we fit the E_g values for different thickness samples by an exponential function as E_g (eV) = 0.5836 × exp(−thickness/3.525) + 1.29 as shown in the inset of Fig. 5(c). Then we extract the E_g values for our samples as 1.48 eV for 3.6 nm, 1.41 eV for 5.4 nm, 1.34 eV for both 8.4 nm and 1.33 eV for the 9.0 nm thick sample. This treatment could help us determine R and D values with better confidence instead of using a constant E_g value. τ is set as 1 ns at room temperature.[26] For MoS_2, it has been documented that the photo-excited electrons have a lifetime of hundreds of picoseconds in few-layer samples and nanoseconds or longer in the thick crystal.[26,45] We first solve the carrier diffusion equation [eqn (1)] and then the heat conduction one with the hot carrier concentration $\Delta N(\boldsymbol{r},t)$ used in the source term.

Here we take the 3.6 nm thick MoS_2 sample for example to discuss the modeling results. In our modeling, we scan the combined space of diffusion coefficient D and interface thermal resistance R to calculate the temperature difference between MoS_2 and c-Si under 20× and 100× objective laser heating. The (D, R) pair giving the temperature difference both agreeing with the 20× and 100× experimental results is taken as the real properties of the sample. Note that in our Raman experiment, the measured temperature rise of both MoS_2 and c-Si are the Raman-intensity weighted average temperature of the sample as $\Delta\bar{T} = \iiint \Delta T I_{Raman} dV / \iiint I_{Raman} dV$. At a location of the sample, the local Raman intensity is proportional to the local laser intensity and the scattered Raman signal multi-reflected in the sample. All these have been considered in our modeling to evaluate the temperature rise of both MoS_2 and the c-Si substrate.

In Fig. 4(a) and (b), we present the calculated averaged temperature difference under two different objective lenses: $\Delta\bar{T}_{20\times}$ and $\Delta\bar{T}_{100\times}$ in the (D, R) space for the 3.6 nm thick MoS_2

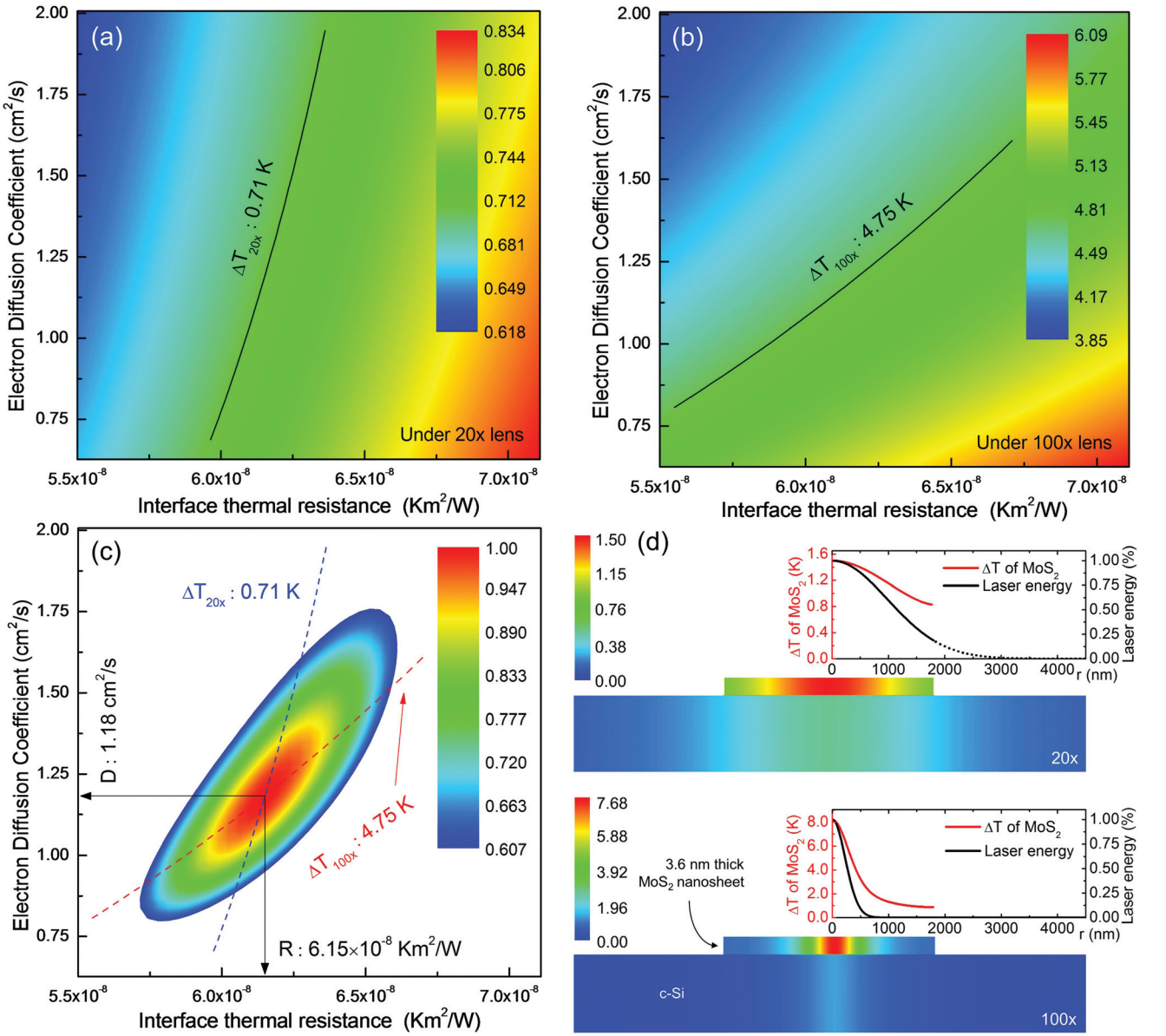

Fig. 4 3D numerical modeling results for the sample with a thickness of 3.6 nm to illustrate the results. The Raman intensity-weighted average temperature difference for different values of the electron diffusion coefficient and interface thermal resistance is shown in (a) under 20× objective and in (b) under 100× objective. The experimentally obtained temperature difference $\Delta\bar{T}_{20\times}$ = 0.71 K at 20× objective and $\Delta\bar{T}_{100\times}$ = 4.75 K at 100× objective are shown in these two figures. (c) Determined D and R as well as the uncertainty region. The normalized probability distribution function (Ψ) contour shows the uncertainty distribution: 0.6065 is for the σ confidence. (d) Calculated temperature rise distribution in the 3.6 nm MoS_2 sample on c-Si substrate under laser heating with 20× and 100× objective lenses using the determined D and R for this sample.

nanosheet. In both cases, the lower electron diffusion coefficient or higher interface thermal resistance implies a higher temperature rise. When D is lower, the heating area will be limited to the laser heating region, resulting in a higher local temperature rise and difference. When R is higher, less heat will dissipate from MoS_2 to the c-Si substrate under the same temperature drop. This will require a higher local temperature rise to dissipate the heat to the substrate. Additionally, in Fig. 4(a) (under the 20× lens), it is evident that the temperature difference is less sensitive to the D change, especially for the lower values of R. However, when the laser spot size reduces (under 100× lens), the sensitivity of $\Delta\bar{T}_{100\times}$ on D changes increases. The physics can be explained as below. The hot carrier diffusion length is $L_D = \sqrt{\tau D} = 0.344\,\mu m$ (based on our measured D for this sample, and detailed later). This is around 1.5 times the laser spot size under 100× lens (r_0 = 0.294 μm). So the hot carriers could diffuse out of the laser spot size more easily and their effect becomes more prominent.

In Fig. 4(a) and (b), for each heating spot size, the experimentally obtained temperature difference (the isolines) could

be satisfied by many different (D, R) pairs. So we could not determine final results based on a single case. To determine D and R, we combine the results from both cases as shown in Fig. 4(c). For the sample of 3.6 nm thick MoS_2, by the cross point of the red ($\Delta\bar{T}_{100\times}$) and blue ($\Delta\bar{T}_{20\times}$) dashed curves, we could determine that D is 1.18 $cm^2\ s^{-1}$ and R is 6.15×10^{-8} K $m^2\ W^{-1}$. To better present the uncertainty of D and R, we calculate the normalized probability distribution function (Ψ) as $\Psi = \exp[-(x-\bar{x})^2/(2\sigma^2)]$, where x, $\bar{x}$, and σ are the variable, its average, and the standard deviation. In the (D, R) space, we have $\Psi_{(D,R)} = \Psi_{\Delta\bar{T}_{100\times}} \cdot \Psi_{\Delta\bar{T}_{20\times}}$ We use the value of $\Psi_{(D,R)}$ = 0.6065 corresponding to the σ confidence in the (D, R) space to show the final result uncertainty. Finally, the deduced R is $6.15^{+0.25}_{-0.25} \times 10^{-8}$ K $m^2\ W^{-1}$ and D is $1.18^{+0.30}_{-0.23}$ $cm^2\ s^{-1}$. The uncertainty of these two values is determined by $\Psi_{(D,R)}$ distribution as shown in Fig. 4(c). For example, to determine the uncertainty of D, by letting $\Psi_{(D,9.26\times10^{-8})} = 0.6065$ in the $\Psi_{(D,R)}$ distribution and fixing the R value, we could obtain D_{min} = 0.950 $cm^2\ s^{-1}$ and D_{max} = 1.48 $cm^2\ s^{-1}$. The final results and the uncertainty for the other three samples are summarized in Table 2 and also plotted in Fig. 5.

Fig. 4(d) shows the calculated temperature rise distribution in the 3.6 nm MoS_2 sample on the c-Si substrate under laser heating with 20× and 100× objective lenses by the determined D and R. For both cases, the temperature rise is quite uniform in the thickness direction in MoS_2 because the sample is very thin. Also the heat conduction/transfer along the thickness direction in MoS_2 is much larger than that in the in-plane direction. Besides, the temperature rise of c-Si is very small because of its high thermal conductivity. For the 3.6 nm thick MoS_2 sample, from the Raman experiment ($\Delta\bar{T} = \chi_P\chi_T^{-1}$), the temperature rise is much smaller than that of MoS_2 as we discussed in the temperature calibration experiment section. So it can easily conduct the heat away from the heating region. Compared with the laser energy distribution, the temperature distribution is out of the laser spot a lot, especially for the case under the 100× objective. As discussed above, the diffusion length L_D is only 1/3 of the laser spot size under the 20× objective and around 1.5 times of that under the 100× objective. This makes the hot carrier diffusion have a significant contribution to our observations under the 100× objective.

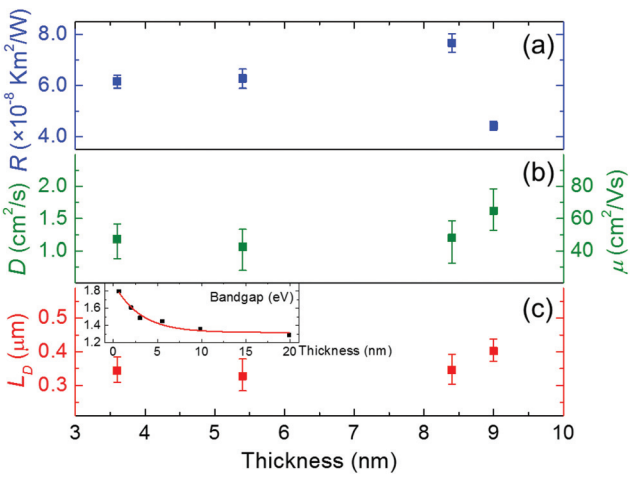

Fig. 5 (a) Interface thermal resistance (R), (b) hot electron diffusion coefficient (D), corresponding electron mobility (μ), and (c) the electron diffusion length (L_D) of four MoS_2 samples. The inset of (c) shows the bandgap energy (dark dot) of thin layers of MoS_2 from Yim *et al.*'s work.[6] We did the exponential fitting (red curve) for the their results to extract E_g values for our four MoS_2 samples. Little thickness effect on hot carrier diffusion was observed here.

As discussed above, during the diffusion process, electrons (e) and holes (h) move as pairs due to the Coulomb attraction between them. Therefore, the measured D is the ambipolar diffusion coefficient, $D = 2D_eD_h/(D_e + D_h)$, where $D_{e(h)}$ is the unipolar diffusion coefficient of electrons (holes).[46] In our optical study, equal numbers of electrons and holes are generated. Besides, the effective masses of electrons and holes of MoS_2 are comparable and even similar.[47] Therefore, the diffusion coefficients for both D_e and D_h are expected to be the same. As a result, the measured value D can be approximately treated as unipolar carrier diffusion coefficients of both electrons and holes. In this thermalized system, the diffusion coefficient is related to the mobility (μ) by the Einstein relation, $D/k_BT = \mu/q$, where k_B, T, and q are the Boltzmann constant, temperature, and the amount of charge of each carrier. For the 3.6 nm thick MoS_2 nanosheets sample, the measured D corresponds to a mobility of μ = 47.4 $cm^2\ V^{-1}\ s^{-1}$. Here, we assume that the carriers have a thermal distribution of 300 K during the diffusion process because the energy relaxation time is only several picoseconds.[26] Our measured μ is very close to the literature values of 30–60 $cm^2\ V^{-1}\ s^{-1}$ for multilayer MoS_2 on SiO_2,[18] and ~70 $cm^2\ V^{-1}\ s^{-1}$ for multilayer MoS_2 on Al_2O_3.[48]

The interface thermal resistance we obtain here is in the order of 6×10^{-8} K $m^2\ W^{-1}$ as summarized in Table 2. They are lower than what we found in previous work, such as the 7.8 nm MoS_2 on c-Si with an R of 1.66×10^{-7} K $m^2\ W^{-1}$.[35] We attribute this mainly to the fact that the samples we prepare here have better interface contact due to our development experience in sample preparation. Tang *et al.* found that the loose (imperfect) contact at the interface could dramatically reduce the interface thermal energy coupling.[49]

4.4 Discussions

As reported before, one approach that could simultaneously extract the thermal conductivity and interface thermal resistance of supported 2D layered material has been developed by exploiting the property of the laser beam.[50] However, that method cannot explain the results we observed in this work because they did not consider the hot carrier diffusion phenomena. For the purpose of non-contact detection, the pump–probe technique has also been applied to study charge carriers in MoS_2 [30] and graphene nanosheets.[15] The biggest difference between the optical and electric measurement of carrier mobility is that we do not need to cover the sample (MoS_2 nanosheet) with a dielectric layer such as HfO_2.[16] The dielectric layer is believed to affect mobility because of the

suppression of Coulomb scattering by the dielectric.[51,52] Nevertheless, our optically measured mobility is still comparable to those with a dielectric top layer. As described above, during the diffusion process, the electron–hole pair moves as a unit so that the pair is electrically neutral. In this case, the pair will not be influenced by the Coulomb scattering.[30]

In our data processing by solving eqn (1) and (2), τ takes 1 ns. The finally determined D is dependent on the τ value. To further elucidate this effect, we use a normalized hot carrier concentration $\xi = \Delta N/\tau$ to re-express eqn (1) and (2) as (by neglecting the thermal activation term):

$$D\tau\nabla^2\xi - \xi + \Phi\alpha = 0, \quad (3)$$

$$k\nabla^2\Delta T + (h\nu - E_g)\Phi\alpha + E_g\xi = 0. \quad (4)$$

From the above equation, it is clear the term $D\tau$ can be determined without the input of other hot carrier properties. The carrier diffusion coefficient D is determined based on the carrier lifetime τ. However, the interface thermal resistance R has no dependence on the carrier lifetime. The lifetime diffusion length of the hot carriers is calculated from D and τ as $L_D = \sqrt{\tau D}$. As summarized in Table 2, for the four samples (3.6 nm, 5.4 nm, 8.4 nm, and 9.0 nm thickness), their L_D are determined as 0.344 μm, 0.327 μm, 0.346 μm, and 0.402 μm, respectively. It is conclusive that the technology developed in this work can firmly determine the lifetime diffusion length of hot carriers. Their diffusion coefficient is dependent on the lifetime data, which needs to be obtained from a separate experiment. A recently published work found that the photocarriers in the C-exciton state are hot carriers with free-carrier properties which could also transport energy.[53] Under our 532 nm (2.33 eV) laser excitation, the high energy C-exciton (transition optical band gap of C-excitonic transition for few-layered MoS_2 is 2.70 eV (ref. 54)) could also be generated by the up-conversion process but with relatively lower possibility than that using a 400 nm (3.10 eV) laser. This C-exciton effect is actually already included in our experimental model because C-excitons will also contribute to the local temperature rise and energy transfer which is probed by Raman spectroscopy to identify the effect of the hot carrier diffusion in our work.

As shown in Table 2 and Fig. 5, the R and D have a relatively high uncertainty, especially for D. This is mainly caused by the uncertainty from the linearly fitting of χ_P and χ_T. Additionally, the little thickness-dependent hot carrier diffusion coefficient we find here may be attributed to the stronger effect of Coulomb scattering or weaker in-plane electron–phonon interaction for thicker samples.[55] As for the sample, we do not reduce the thickness of MoS_2 nanosheets to a single layer due to sample preparation difficulty. Under an optical microscope, the single-layered MoS_2 has very weak visibility on the c-Si substrate compared with that on the SiO_2 substrate. This makes it extremely difficult to identify it for Raman study. Besides, for single-layered MoS_2, its larger bandgap (~1.8 eV) could potentially reduce electron mobility[56] and it is very sensitive to air exposure which is so far believed to make it have a lower mobility.[57] Both experiment and analytic modeling have shown that multilayered MoS_2 devices could have a higher mobility and density of states under the same dielectric environment. Also, they have a higher current limit and better manufacturability compared with single layer devices.[58]

5. Conclusions

In summary, we have developed a novel technology for the determination of both the hot carrier diffusion coefficient (D) and the interface thermal resistance (R) of sub-10 nm virgin mechanically exfoliated MoS_2 nanosheets on the c-Si substrate. The hot carrier effect on heat conduction by photon excitation, diffusion, and recombination could significantly extend the heating area size, especially when the laser focal spot size is comparable to the hot carrier diffusion length. The laser focal spot size was varied from 0.294 μm to 1.14 μm to change its effect in heat conduction, and the resulting temperature rise was measured by Raman spectroscopy. For our four sub-10 nm MoS_2 samples (3.6, 5.4, 8.4 and 9.0 nm), their hot carrier diffusion coefficient was measured as $1.18^{+0.30}_{-0.23}$, $1.07^{+0.37}_{-0.26}$, $1.20^{+0.34}_{-0.27}$ and $1.62^{+0.30}_{-0.23}$ $cm^2\ s^{-1}$ under a 1 ns hot carrier lifetime. A little thickness effect on hot carrier diffusion was observed. In fact, this technology can firmly determine the hot carrier diffusion length without knowledge of the lifetime. The four samples' hot carrier diffusion length was determined as $0.344^{+0.041}_{-0.036}$ (3.6 nm), $0.327^{+0.052}_{-0.043}$ (5.4 nm), $0.346^{+0.046}_{-0.042}$ (8.4 nm), and $0.402^{+0.036}_{-0.030}$ μm (9.0 nm). The hot carrier diffusion coefficient study is conducted without applying an electric field or electrical contact so the results could reflect the intrinsic properties of virgin 2D materials. We believe this non-contact and non-invasive technique could also be used for carrier transport and interface energy coupling study of other 2D materials. There have been only a few reports regarding hot carrier transport studies for MoS_2 nanosheets or the methods to exclude the potential influence on the transport measurement caused by the electrode. Also the results point out that for photon-excitation based energy transport study in 2D materials, hot carrier diffusion could play a big role in affecting the results, especially when the excitation size is comparable to the hot carrier diffusion length.

Acknowledgements

Support of this work by National Science Foundation (CBET1235852, CMMI1264399), Department of Energy (DENE0000671, DE-EE0007686), and Iowa Energy Center (MG-16-025, OG-17-005) is gratefully acknowledged.

References

1 Q. H. Wang, K. Kalantar-Zadeh, A. Kis, J. N. Coleman and M. S. Strano, *Nat. Nanotechnol.*, 2012, 7, 699–712.

2 A. P. Gaur, S. Sahoo, M. Ahmadi, M. J.-F. Guinel, S. K. Gupta, R. Pandey, S. K. Dey and R. S. Katiyar, *J. Phys. Chem. C*, 2013, **117**, 26262–26268.
3 X. Huang, Z. Yin, S. Wu, X. Qi, Q. He, Q. Zhang, Q. Yan, F. Boey and H. Zhang, *Small*, 2011, **7**, 1876–1902.
4 W. Wu, L. Wang, Y. Li, F. Zhang, L. Lin, S. Niu, D. Chenet, X. Zhang, Y. Hao and T. F. Heinz, *Nature*, 2014, **514**, 470–474.
5 K. F. Mak, C. Lee, J. Hone, J. Shan and T. F. Heinz, *Phys. Rev. Lett.*, 2010, **105**, 136805.
6 C. Yim, M. O'Brien, N. McEvoy, S. Winters, I. Mirza, J. G. Lunney and G. S. Duesberg, *Appl. Phys. Lett.*, 2014, **104**, 103114.
7 O. Lopez-Sanchez, D. Lembke, M. Kayci, A. Radenovic and A. Kis, *Nat. Nanotechnol.*, 2013, **8**, 497–501.
8 A. Polman and H. A. Atwater, *Nat. Mater.*, 2012, **11**, 174–177.
9 Y. Leblebici and S.-M. S. Kang, *Hot-carrier reliability of MOS VLSI circuits*, Springer Science & Business Media, 2012.
10 Z. Lang, X. Zheng, C. Shao-Wen, D. Gang, K. Jin-Feng and L. Xiao-Yan, *Chin. Phys. Lett.*, 2014, **31**, 027301.
11 S. Kim, A. Konar, W.-S. Hwang, J. H. Lee, J. Lee, J. Yang, C. Jung, H. Kim, J.-B. Yoo and J.-Y. Choi, *Nat. Commun.*, 2012, **3**, 1011.
12 H. Lin, S. Xu, Y.-Q. Zhang and X. Wang, *ACS Appl. Mater. Interfaces*, 2014, **6**, 11341–11347.
13 J. C. Song, M. S. Rudner, C. M. Marcus and L. S. Levitov, *Nano Lett.*, 2011, **11**, 4688–4692.
14 F. Bonaccorso, Z. Sun, T. Hasan and A. Ferrari, *Nat. Photonics*, 2010, **4**, 611–622.
15 B. A. Ruzicka, S. Wang, L. K. Werake, B. Weintrub, K. P. Loh and H. Zhao, *Phys. Rev. B: Condens. Matter*, 2010, **82**, 195414.
16 B. Radisavljevic, A. Radenovic, J. Brivio, i. V. Giacometti and A. Kis, *Nat. Nanotechnol.*, 2011, **6**, 147–150.
17 J. H. Strait, P. Nene and F. Rana, *Phys. Rev. B: Condens. Matter*, 2014, **90**, 245402.
18 W. Bao, X. Cai, D. Kim, K. Sridhara and M. S. Fuhrer, *Appl. Phys. Lett.*, 2013, **102**, 042104.
19 G. Nazir, M. F. Khan, V. M. Iermolenko and J. Eom, *RSC Adv.*, 2016, **6**, 60787–60793.
20 A. D. Semenov, G. N. Gol'tsman and R. Sobolewski, *Supercond. Sci. Technol.*, 2002, **15**, R1.
21 X. Shen, H. Wang and T. Yu, *Nanoscale*, 2013, **5**, 3352–3358.
22 W. Bao, G. Liu, Z. Zhao, H. Zhang, D. Yan, A. Deshpande, B. LeRoy and C. N. Lau, *Nano Res.*, 2010, **3**, 98–102.
23 S. Kang, H. C. P. Movva, A. Sanne, A. Rai and S. K. Banerjee, *J. Appl. Phys.*, 2016, **119**, 124502.
24 N. Kumar, J. He, D. He, Y. Wang and H. Zhao, *J. Appl. Phys.*, 2013, **113**, 133702.
25 R. Wang, B. A. Ruzicka, N. Kumar, M. Z. Bellus, H.-Y. Chiu and H. Zhao, *Phys. Rev. B: Condens. Matter*, 2012, **86**, 045406.
26 H. Shi, R. Yan, S. Bertolazzi, J. Brivio, B. Gao, A. Kis, D. Jena, H. G. Xing and L. Huang, *ACS Nano*, 2013, **7**, 1072–1080.
27 M. Nestoros, B. C. Forget, C. Christofides and A. Seas, *Phys. Rev. B: Condens. Matter*, 1995, **51**, 14115.
28 C. Christofides, A. Othonos and E. Loizidou, *J. Appl. Phys.*, 2002, **92**, 1280–1285.
29 C. Christofides, F. Diakonos, A. Seas, C. Christou, M. Nestoros and A. Mandelis, *J. Appl. Phys.*, 1996, **80**, 1713–1725.
30 R. Fivaz and E. Mooser, *Phys. Rev.*, 1967, **163**, 743.
31 M. S. Shur, *Handbook series on semiconductor parameters*, World Scientific, 1996.
32 J. Suh, T.-E. Park, D.-Y. Lin, D. Fu, J. Park, H. J. Jung, Y. Chen, C. Ko, C. Jang and Y. Sun, *Nano Lett.*, 2014, **14**, 6976–6982.
33 J. Linnros, *J. Appl. Phys.*, 1998, **84**, 275–283.
34 E. X. Pérez, *Design, fabrication and characterization of porous silicon multilayer optical devices*, Universitat Rovira i Virgili, 2008.
35 P. Yuan, C. Li, S. Xu, J. Liu and X. Wang, *Acta Mater.*, 2017, **122**, 152–165.
36 H. Li, J. Wu, Z. Yin and H. Zhang, *Acc. Chem. Res.*, 2014, **47**, 1067–1075.
37 M. A. Meitl, Z.-T. Zhu, V. Kumar, K. J. Lee, X. Feng, Y. Y. Huang, I. Adesida, R. G. Nuzzo and J. A. Rogers, *Nat. Mater.*, 2006, **5**, 33–38.
38 P. Nemes-Incze, Z. Osváth, K. Kamarás and L. Biró, *Carbon*, 2008, **46**, 1435–1442.
39 A. Taube, J. Judek, A. Łapińska and M. Zdrojek, *ACS Appl. Mater. Interfaces*, 2015, **7**, 5061–5065.
40 S. Sahoo, A. P. Gaur, M. Ahmadi, M. J.-F. Guinel and R. S. Katiyar, *J. Phys. Chem. C*, 2013, **117**, 9042–9047.
41 L. Su, Y. Zhang, Y. Yu and L. Cao, *Nanoscale*, 2014, **6**, 4920–4927.
42 N. A. Lanzillo, A. G. Birdwell, M. Amani, F. J. Crowne, P. B. Shah, S. Najmaei, Z. Liu, P. M. Ajayan, J. Lou and M. Dubey, *Appl. Phys. Lett.*, 2013, **103**, 093102.
43 J. Liu, G.-M. Choi and D. G. Cahill, *J. Appl. Phys.*, 2014, **116**, 233107.
44 M. Neuberger, in *Handbook of Electronic Materials*, Springer, 1971, pp. 5.
45 H. Wang, C. Zhang and F. Rana, *Nano Lett.*, 2014, **15**, 339–345.
46 D. A. Neamen, *Semiconductor physics and devices*, McGraw-Hill Higher Education, 2003.
47 L. Liu, S. B. Kumar, Y. Ouyang and J. Guo, *IEEE Trans. Electron Devices*, 2011, **58**, 3042–3047.
48 W. Choi, M. Y. Cho, A. Konar, J. H. Lee, G. B. Cha, S. C. Hong, S. Kim, J. Kim, D. Jena and J. Joo, *Adv. Mater.*, 2012, **24**, 5832–5836.
49 X. Tang, S. Xu, J. Zhang and X. Wang, *ACS Appl. Mater. Interfaces*, 2014, **6**, 2809–2818.
50 J. Judek, A. P. Gertych, M. Świniarski, A. Łapińska, A. Dużyńska and M. Zdrojek, *Sci. Rep.*, 2015, **5**, 12422.
51 M. Ono, T. Ishihara and A. Nishiyama, *IEEE Trans. Electron Devices*, 2004, **51**, 736–740.

52 J. Yang, Z. Xia, G. Du, X. Liu, R. Han and J. Kang, *2006 8th International Conference on Solid-State and Integrated Circuit Technology Proceedings*, 2006, pp. 1315–1317.
53 L. Wang, Z. Wang, H.-Y. Wang, G. Grinblat, Y.-L. Huang, D. Wang, X.-H. Ye, X.-B. Li, Q. Bao and A.-S. Wee, *Nat. Commun.*, 2017, **8**, 13906.
54 Y. Yu, Y. Yu, Y. Cai, W. Li, A. Gurarslan, H. Peelaers, D. E. Aspnes, C. G. Van de Walle, N. V. Nguyen and Y.-W. Zhang, *Sci. Rep.*, 2015, **5**, 16996.
55 M.-W. Lin, I. I. Kravchenko, J. Fowlkes, X. Li, A. A. Puretzky, C. M. Rouleau, D. B. Geohegan and K. Xiao, *Nanotechnology*, 2016, **27**, 165203.
56 S.-L. Li, K. Komatsu, S. Nakaharai, Y.-F. Lin, M. Yamamoto, X. Duan and K. Tsukagoshi, *ACS Nano*, 2014, **8**, 12836–12842.
57 D. Lembke, A. Allain and A. Kis, *Nanoscale*, 2015, **7**, 6255–6260.
58 R. Yang, Z. Wang and P. X.-L. Feng, *Nanoscale*, 2014, **6**, 12383–12390.